Materials Research. 2022; 25:e20220179
DOI: https://doi.org/10.1590/1980-5373-MR-2022-0179

Pitting and Crevice Corrosion Behavior of the Duplex Stainless Steel UNS S32205 Welded by Using the GTAW Process

Yamid E. Nuñez de la Rosa[a]* **, *Oriana Palma Calabokis***[a] **, *Gloria M. Pena Uris***[b]**,**

Paulo César Borges[a]

[a]*Universidade Tecnológica Federal do Paraná (UTFPR), 81280-340, Curitiba, PR, Brasil.*
[b]*Universidade de Vigo, Centro de Investigación en Tecnoloxías, Enerxía e Procesos Industriais (CINTECX), Enxeñaría da Corrosión e Materiais (ENCOMAT), 36310, Vigo, Spain.*

Received: April 01, 2022; Revised: August 28, 2022; Accepted: October 19, 2022

This study investigated the pitting and crevice corrosion behavior of the gas tungsten arc welding (GTAW) process in the UNS S32205 according to industrial parameters. Results revealed that the welding process presented a weld metal chemical composition similar to the base metal and an adequate balance of the austenite and ferrite phases. No relevant variation in the hardness was observed and XRD spectra did not identify the presence of deleterious phases in the weld bead. Cyclic polarization tests revealed similarities between welded and base metal samples (20±2°C, NaCl 3.5% wt.). When comparing the behavior obtained in the crevice, and pitting tests, a decrease in the corrosion resistance was observed in the presence of a crevice former. The SEM-EDS proved that the attack occurred mainly in secondary austenites. Profilometry measurements revealed that the crevice corrosion in the weld region was deeper than in the base metal. However, considering the welded samples as a unit, making no difference between regions: weld metal, HAZ, and base metal, the average crevice corrosion depth was comparable to that of the base metal samples. Finally, it was concluded that the welding process used for the UNS S32205 steel did not harm its corrosion resistance.

Keywords: *DSS, UNS S32205, weld, GTAW, pitting corrosion, crevice corrosion.*

1. Introduction

Duplex stainless steels (DSS) belong to a family of steels that present a two-phase microstructure with roughly equal proportions of austenite (γ) and ferrite (α) at room temperature[1-4] (Figure 1). This balance between the phases results in an interesting combination of properties, namely, mechanical resistance, toughness, corrosion resistance, and weldability[5-8].

The DSS UNS S32205 (3%Mo, 22%Cr, and 5%Ni) is mainly used in the chemical industry, oil transportation, food, paper and cellulose[9-13]. In these areas, pipes, tanks, and other components require a welding process that does not alter their mechanical and corrosion resistance properties. The welding processes that are mostly used in these steels according to the literature are: GMAW (Gas Metal Arc Welding)[9,14,15], FCAW (Flux-Cored Arc Welding)[16,17], SAW (Submerged Arc Welding)[18], SMAW (Shield Metal Arc Welding)[13,19], and GTAW (Gas Tungsten Arc Welding)[17,20-22].

All the processes listed above, depending on the welding conditions can generate undesirable changes in the ferrite-austenite ratio and/or in the distribution of the alloying elements in the DSS weld metal (WM) and in the HAZ. These could be a consequence of the thermal gradients resulting from the alteration of the welding speed, current, and tension[1,23-25]. Unsuitable heat input can promote the formation of deleterious phases that alters the hardness and harms the corrosion resistance[26]. To prevent such undesirable changes, some studies suggest that the heat input recommended for the DSS UNS S32205 must be around 0.5 kJ/mm up to 2.5 kJ/mm[13,14,23,27-30].

The GTAW process is one of the most popular DSS welding methods[31]. This process outstands for providing a better ferrite-austenite ratio (around 50% of each) when compared to other welding processes, according to the standards TAPPI TIP 0402-29 and Norsok M-601, 2016[25,29,32]. However, every welding process generates microstructural differences that might hamper the material corrosion resistance in the conditions in which DSS is used[33]. Microstructural characteristics depend on the choice of the welding procedure and the process parameters (current, potential, speed, heat input, and cooling rate), the filler material, the materials to be welded, and the shielding gas. As a result, welded DSS evaluation focuses on the investigation of pitting corrosion resistance in chloride environments, mainly employing cyclic potentiodynamic polarization[14,34-36] and critical pitting temperature (CPT ASTM G150)[35,37]. Also, other techniques have been evaluated such as the modified double loop electrochemical potentiokinetic reactivation[38], electrochemical impedance[33], and immersion tests[13]. A study put forward by Zhou et al.[5] that investigated 2101 lean duplex stainless steel welded using the TIG (Tungsten Inert Gas) process evaluated the material susceptibility to generalized, pitting, and transpassive corrosion with a single electrochemical

---

*e-mail: yamid@alunos.utfpr.edu.br

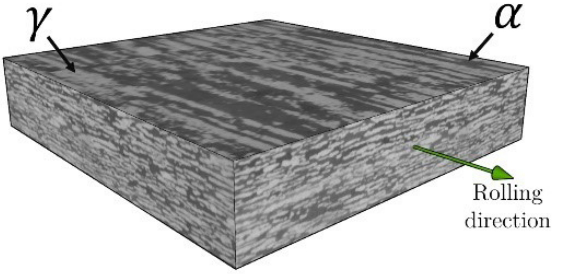

Figure 1. DSS UNS S32205 microstructure, ferrite phase (α: darker) and austenite phase (γ: lighter).

technique known as bipolar electrochemistry technique. Zhou et al.[5] revealed that the austenite morphologies were preferentially attacked by pitting and transpassive corrosion. Besides, the un-balanced microstructure, the formation of deleterious phases, and the high chemical composition heterogeneity weaken the corrosion resistance in different DSS welding joints, as reported in previous works[5,6,34,36-38].

Studies on localized corrosion in welded DSS focus mainly on pitting corrosion. However, there are several practical cases of geometries that lead to crevice corrosion such as gaskets, washers, screw heads, flanged pipes, pipe support brackets, lap joints, and surface deposits that make this type of corrosion less evident and often neglected[5,39]. In fact, weld beads are surface heterogeneities around which liquids can be retained, which favor crevice corrosion[5,39]. Among the studies on welded DSS, only Zhou et al.[5] reported crevice corrosion in the interface between the sample and the lacquer covering it without studying it systematically. Taking into consideration that the DSS UNS S32205 welding processes are so common in the industrial the main purpose of this study aimed to investigate the pitting and crevice corrosion resistance in a NaCl 3.5% wt. of the welded DSS UNS S32205 using the GTAW process.

2. Experimental Procedure

2.1. Material and welding process

Plates of DSS UNS S32205 with 4 mm in thickness, 300 mm in length and 50 mm in width, were used as base materials. The GTAW technique was utilized in preparing DSS joints. Argon (12-20 L/min) was used as shielding gas in the 1G position and a stainless steel ER-2209 (Lincoln®) wire (Ø=2.5 mm) was used as consumable electrode. Welding was carried out using a current of 110-200 A and arc voltage of 23-28 V. The welds were made by a specialized welding company that works for the Brazilian pulp and paper industries.

Chemical composition of the base material and weldments was determined by Positive Material Identification (PMI) technique: (Olympus-DELTA Premium) and Scanning Electron Microscopy (SEM) and Energy Dispersive X-ray Spectroscopy (EDS): (Zeiss-EVO MA15) was also used to perform analysis of sample surface.

Two types of samples were analyzed: untreated UNS S32205 sheet samples, identified as BM (base metal) and samples with weld joint called BM-WM (these samples containing base metal, heat affected zone, and weld metal region). The surfaces were ground with emery papers up to #1200 mesh and the samples were cold mounted in epoxy resin with a copper wire assembled for electric contact for the electrochemical tests (pitting and crevice corrosion tests).

2.2. Microstructural and microhardness analyses

BM and BM-WM samples were polished with 1 μm alumina and etched with modified Behara (100 ml H_2O + 20 ml HCl + 0.4 g potassium metabisulfite) at room temperature for 600 s[40]. The BM, HAZ, and WM regions were analyzed by optical microscopy (OM) using a Olympus-BX51 and the free software *Image J.* Ten micrographs were randomly obtained for each region along the welded sheets in order to compute the average phases percentage in each zone.

The existence of possible harmful phases was determined by X-ray diffraction patterns using a Shimadzu XRD-7000 diffractometer under CuK-α (λ = 1,54060 Å) radiation, operating at 40 kV/30 mA. The scanning range was: 20°–120°, with a step width of 0.02° and 1 s per step as collecting time. The Bragg angles, 2θ, and the interplanar spacing (d-spacing) corresponding to the detected peaks were compared with the standard values from the International Centre for Diffraction Data's Powder Diffraction File (JCPDS- ICDD).

The microhardness determination of the welded samples was measured, carried out at the top and perpendicular to the weld bead. The equipment used was a Shimadzu Dynamic Ultra Micro Hardness Testers DUH-21S, using a load of 50 g for 10 s and a space between indentations of 0.5 mm according to the ISO 14577-1 standard.

2.3. Cyclic Polarization tests (CP)

Aiming to determine the pitting corrosion behavior, CP tests were carried out in a three-electrode electrochemical cell. The working electrode (WE) was the mounted sample (4 cm^2), the reference electrode (RE) was a KCl saturated silver-silver chloride (Ag-AgCl/sat) electrode, and the auxiliary electrode (AE) was a graphite rod. All electrodes are connected to the potentiostat (PalmSens, model EmStat3; software PSTrace 5). Each test started after the open circuit potential (OCP) stabilization, carried out for an hour. Next, a potential scanning was performed in the anodic direction –0.2 V respecting the OCP potential up to the 1.7 V potential (vs Standard Hydrogen Electrode, SHE) where the polarization was reversed to the cathodic direction. The tests were carried out at 20 °C in a NaCl 3.5% wt. and a 1 mV/s scanning rate. All potentials presented in this study has been converted into the SHE.

2.4. Crevice corrosion tests

The susceptibility to crevice corrosion was evaluated using a PD-PS-PD test consisting of three consecutive stages, as suggested by Palma et al.[41]. After OCP stabilization for an hour, a potentiodynamic (PD) polarization stage, scanning potential from –0.2 V respecting the OCP to 1.5 V (vs. SHE) at 1 mV/s. Immediately afterward, the potentiostatic (PS) stage is performed, holding 1.5 V for an hour. Finally, a reverse scanning in the cathodic direction is performed (PD stage).

The mounted sample and the crevice former were placed in a corrosion cell devised by Palma Calabokis et al.[41], as shown below (Figure 2).

The position of the samples avoids the deposition of the corrosion products on the sample surface. Constant contact pressure of 508 kPa was imposed between the crevice former and the sample surface, using standardized masses of 3 kg, and, as a result, the crevice mouth standardization was guaranteed in all tests.

2.5. *Surface analysis after the crevice corrosion tests*

After the corrosion tests, the samples were cleaned in an ultrasound bath with ethyl alcohol (70%). The surfaces were analyzed using optical microscopy, stereoscopic microscopy, scanning electron microscopy + EDS, and 2D contact profilometry.

3. Results

3.1. *Chemical composition*

Table 1 shows the average weight percentages (wt.%) of the main alloying elements. Using the PMI technique, the percentages were determined in five different points of the base metal and weld metal regions of welded samples. Also, Table 1 shows the nominal composition of UNS S32205 (ASTM A240) and the composition of the consumable wire indicated in the supplier datasheet for comparison reasons. The distribution of the alloying elements between the austenite and ferrite phases was assessed by SEM-EDS, performing 28-point measurements in the weld metal zone. Average results are shown in Table 1.

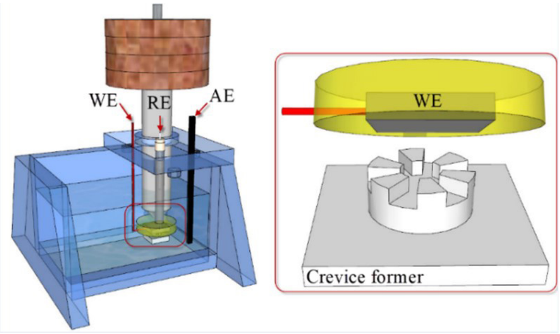

Figure 2. Scheme of the corrosion cell and crevice former used in the crevice corrosion tests (Adapted from Palma Calabokis et al., 2021[41]).

As verified from Table 1, while the alloying weight percentage of the main alloying elements in the base metal is close to the nominal values (according to the ASTM A240 standard), this percentage rises slightly in the welded area due to the contribution from the consumable electrode (ER-2209).

The distribution of the elements was rather uniform between austenite and ferrite in the weld metal. Although a slight concentration of Cr and Mo is observed in the ferrite and of Ni in the austenite, the difference is very small: it falls within the range of dispersion of the measurements. These results agree with those reported by Geng et al.[20], Zhang et al.[42], and Zhang et al.[38], who studied the double and single-pass GTAW and the FCAW welding process in the DSS UNS S31803, respectively.

3.2. *X-ray diffraction*

Figure 3 presents the X-ray patterns obtained from the base metal (blue) and weld metal (red) regions of the BM-WM samples. Note that both spectra show the same diffraction peaks characteristic of ferrite (α) and austenite (γ) crystalline structures, with very little difference in relative intensity. No peaks corresponding to deleterious phases were found (such as sigma phase, chi phase, chromium nitrides).

3.3. *Phase quantification*

The microstructure of the DSS UNS S32205 in the three analyzed regions is shown in Figure 4: a) base metal

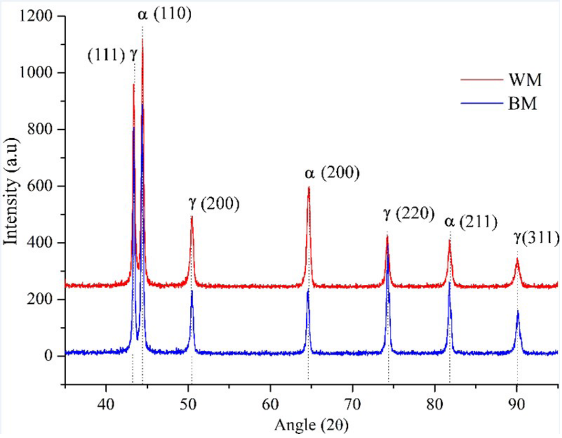

Figure 3. X-ray diffraction patterns for DSS UNS S32205 samples in the base metal (BM; blue) and in the weld metal (WM; red) regions and corresponding Miller indexes.

Table 1. Nominal composition of DSS UNS S32205 (ASTM A240) and the consumable electrode (datasheet) compared to the average values determined by PMI technique and elemental distribution between phases in the weld zone (SEM-EDS).

	Cr wt.%	Ni wt.%	Mo wt.%	Mn wt.%
UNS S32205 (ASTM A240)	22.0 – 23.00	4.5 – 6.5	3.0 – 3.5	2.0
Base metal (PMI)	22.17 ± 0.24	5.72 ± 0.03	3.19 ± 0.01	1.23 ± 0.05
Electrode ER-2209 (Datasheet)	23.3	8.5	3.38	1.43
Weld metal (PMI)	22.95 ± 0.25	7.88 ± 0.22	3.40 ± 0.04	1.64 ± 0.23
Austenite in the weld metal (SEM-EDS)	22.46 ± 0.93	7.48 ± 0.71	3.21 ± 0.36	1.49 ± 0.11
Ferrite in the weld metal (SEM-EDS)	23.27 ± 0.23	6.86 ± 0.48	3.59 ± 0.22	1.47 ± 0.11

(BM), b) heat-affected zone (HAZ), and c) weld metal zone (WM). In all micrographs, the darker areas correspond to the ferritic matrix and the lighter areas correspond to the austenitic phase.

Figure 4a shows the typical DSS microstructure where islands of austenite (γ), elongated in the rolling direction, are surrounded by the continuous ferrite phase (α). The micrograph in Figure 4b presents the optical microstructure of the transition region of the welded DSS UNS S32205 from the base metal, on the left, to the weld region on the right, where the microstructure is similar to that of Figure 4c. In the middle, an intermediate microstructure, corresponding to the HAZ, can be observed.

Figure 4c corresponds to the weld metal region, where different austenite morphologies are seen: grain boundary austenite (GBA), Widmanstätten austenite (WA), and intragranular austenite (IGA). These are morphologies characteristic of the solidification process during cooling[14,40,43]. From the molten metal, only α phase is directly formed, and austenite is subsequently originated from ferrite transformation in the solid-state. GBA nucleates at the grain boundaries as can be seen in Figure 4b, c, and can be continuous or discontinuous depending on the cooling speed. WA nucleates at the ferrite or GBA grain boundaries, and grows aligned along specific planes that are parallel one to another. Finally, IGA is identified as small islands scattered along with the ferritic matrix[14,44] as can be seen in Figure 4b, c.

Figures 4d-f presents the binary images of Figure 4a-c., which have been processed using the free software *Image J* to quantify the phases. Table 2 shows the results obtained from this analysis with corresponding standard deviations. The quantitative analysis of the volumetric fractions of the ferrite and austenite phases in the base metal (BM) showed proportions close to the expected (~50%). The TAPPI TIP 0402-29 standard[45] establishes that the phase balance in the weld metal zone must have at least 30% ferrite. At the

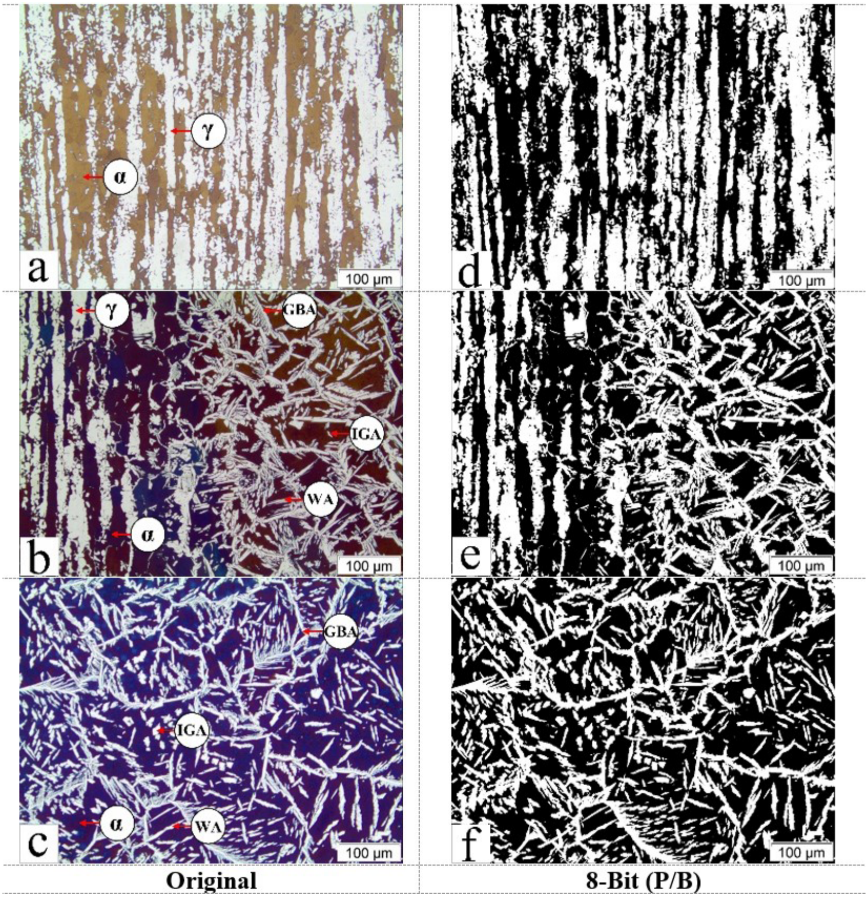

Figure 4. Optical micrograph of the surface top etched with modified Behara for 600 s in the: a. BM, b. HAZ, and c. WM. d-f. Binary images corresponding to the images a-c.

Table 2. Percentage of austenite and ferrite phases in BM, BM-HAZ-WM, and WM determined at the top of the DSS UNS S32205 welded samples.

BM region		BM-HAZ-WM region		WM region	
γ	α	γ	α	γ	α
52% ± 4%	48% ± 4%	35% ± 4%	65% ± 4%	45%± 2%	55%± 2%

same time, the Norsok M-601 standard[46], establishes that the austenite fraction cannot be below 25%. Considering the results presented in Table 2, the phase balance is within the limits set forth in both standards. The phase quantification in the welded samples (Table 2) revealed that the welding process used favored a balanced microstructure between ferrite and austenite as well as a similar distribution of alloy elements in the weld metal and the base metal (Table 1) as provided for in the TAPPI TIP 0402-29[45] and Norsok M-601[46] standards. On the other hand, in the BM-HAZ-WM transition (Table 2), a slight increase in the ferrite content was observed, which is usually associated with the material heating and cooling cycles during welding, in agreement with those obtained in other DSS studies[15,38,47]. However, this phase balance at the BM-HAZ-WM transition meets the requirements of the standards listed above.

3.4. Microhardness

Microhardness indentations carried out along a direction perpendicular to the weld bead are shown in Figure 5. The microhardness profile was carried out at the top of the BM-WM samples starting from the base metal, going through the weld bead, and reaching the base metal again.

Figure 6 shows the curve of the Vickers microhardness ($HV_{0.05}$) values measured along the profile as a function of distance. From this figure, it is observed that the hardness profile shows that the welding process used in the DSS UNS S32205 was adequate favorable since the hardness values in the weld bead and HAZ transition are close to the BM. The maximum and minimum values in these measurements were 343 $HV_{0.05}$ and 293 $HV_{0.05,}$ respectively with an average value of 328 ± 11 $HV_{0.05}$, in agreement with Tahaei et al.[22]. Those authors confirmed that uniform hardness values along the regions (BM-HAZ-WM) showed a direct relation with a suitable balance between microstructural phases and their chemical composition, without deleterious phases using the TIG welding process in duplex steel UNS S32304[22].

3.5. Cyclic polarization tests (CP)

Figure 7 shows the most representative CP curves obtained in the base metal (blue), in the welded samples (red), and the variation of OCP with immersion time. Table 3 lists the average values of the parameters of interest corresponding to the triplicates of these tests. Student T-tests were carried out (3 samples of each condition; confidence interval 95%) to confirm whether there were statistical differences between the average parameters (listed in Table 3) of the BM and BM-WM specimens. Therefore, the E_R and E_{bd} potentials were confirmed as statistically equal in both conditions. However, the BM condition presented more noble values for the E_{Corr} potential when compared to the BM-WM, which suggests the BM greater resistance to generalized corrosion[43]. In addition, the passivation current density lower value (i_{pass}) in the BM suggests that the passive layer formed on them is more protective than that formed on the welded specimens. Also, the corrosion current (i_{corr}) and, consequently, the corrosion rate was lower in BM-WM. In general terms, the electrochemical behavior was not harmed by the welding process when compared to the results reported by Zhou et al.[5], Shin et al.[36], Geng et al.[20], and Tavares et al.[48] on DSS welding. In particular, Zhou et al.[5], Geng et al.[20], and Tavares et al.[48] associated the differences of corrosion susceptibility with changes in phase fraction and local weld chemistry of the DSS GTAW joints. In the present work, the selected parameters for the GTAW welding process performed on DSS UNS S32205 have led to a microstructure almost balanced in austenite-ferrite in the welded joint, with no deleterious phases present such as intermetallic phases, carbides, or nitrides. The presented results of chemical composition, XRD, and the balance microstructure in the welded material meet the requirements of the standards, therefore, a good corrosion resistance of the welded union can be expected.

3.6. Crevice corrosion tests (PD-PS-PD)

The susceptibility to crevice corrosion was evaluated in a specially designed corrosion cell, using a PTE crevice former with 6 crevice slots, by a PD-PS-PD method as it was previously indicated. Figure 8 shows the most representative curves of the crevice corrosion behavior tests and their respective OCP in the BM and the welded piece BM-WM. Table 4 presents the mean values and standard deviations

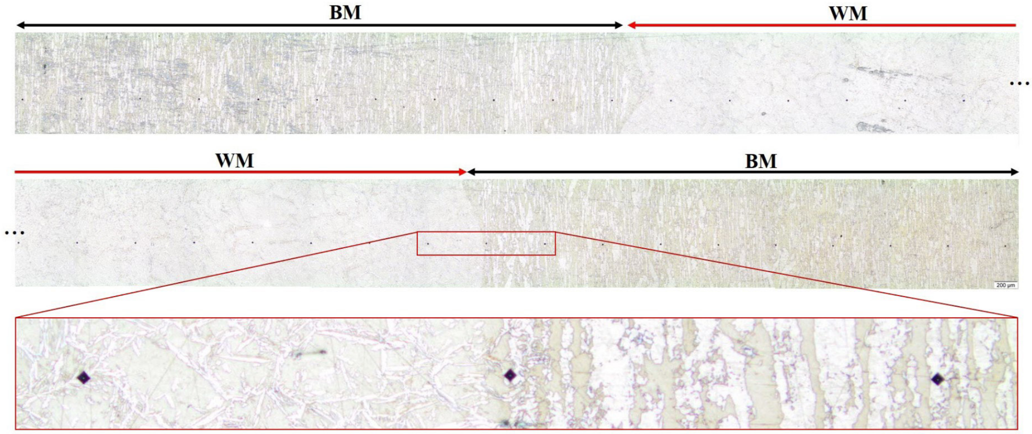

Figure 5. Microhardness profile ($HV_{0.05}$) carried out along the surface of the welded samples, perpendicular to the weld bead. Indentations were performed every 0.5 mm.

of the parameters of interest corresponding to triplicate samples. As in section 3.5, statistical analyses were carried out of both conditions, which revealed that only the mean values of potential E_{bd} differed between BM and BM-WM. The remaining parameters of interest (Table 4) were statistically similar, which shows that the crevice corrosion behavior was not influenced by the welding process, except the breakdown potential.

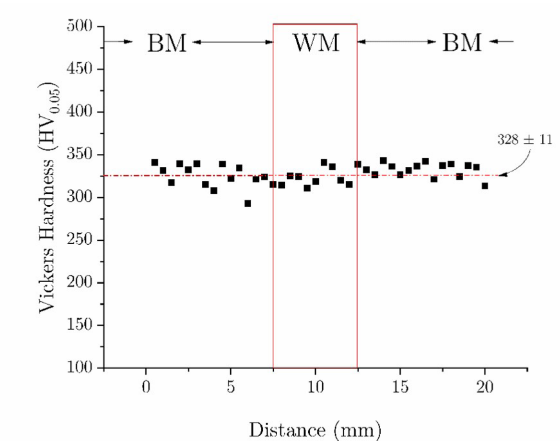

Figure 6. Microhardness values ($HV_{0.05}$) as a function of the distance (mm), indentations were carried out every 0.5 mm.

In addition, when comparing the crevice test values (Table 4) with those obtained in the CP tests (Table 3) a general reduction in the potentials E_R, E_{bd}, and E_{Corr} was observed in both BM and BM-WM as well as an increase in the corrosion and passivation current densities, because of the reactions that occur due to the crevice former contact.

Figure 9 shows two representative curves of the current density as a function of time in the second step of the crevice corrosion tests (potentiostatic polarization, PS). It could be noticed that the current density keeps increasing throughout the test time and showed similar values for both conditions investigated. Therefore, in the PS step, the welded material showed a localized crevice corrosion behavior comparable to the base material, which had been correlated with the same repassivation potential values E_R (Table 4).

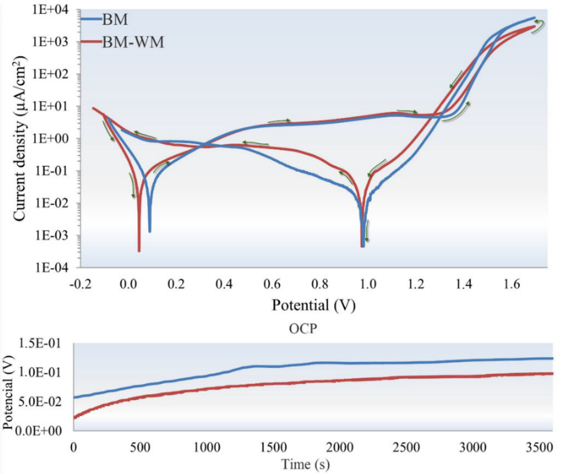

Figure 7. Cyclic polarization curves in BM and BM-WM samples in NaCl 3.5% solution (20 ± 2 °C, 1 mV/s), and their corresponding OCP.

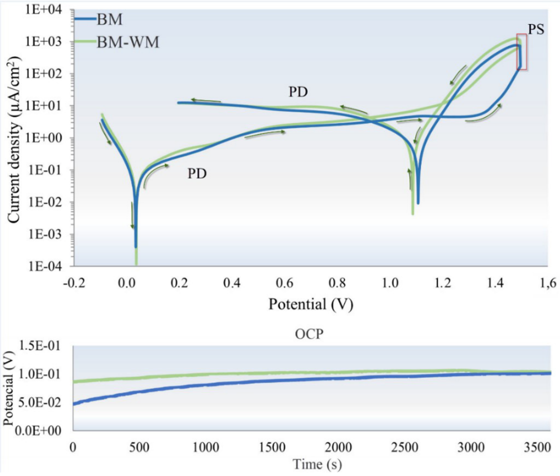

Figure 8. Crevice corrosion tests curves in BM and BM-WM in NaCl 3.5% solution (20 ± 2 °C), and their corresponding OCP.

Table 3. Mean values and standard deviations of the repassivation potential (E_R), breakdown potential (E_{bd}), passivation current density (i_{pass}), corrosion current density (i_{Corr}), corrosion potential (E_{Corr}) and corrosion rate (C_0) of triplicate CP tests in BM and BM-WM in NaCl 3.5% wt. (20 ± 2 °C).

		E_R (V)	E_{bd} (V)	i_{pass} (µA/cm²)	i_{Corr} (µA/cm²)	E_{Corr} (V)	C_0 (mm/ano)
BM	$\bar{x}$	1.310	1.384	2.715	7.43×10^{-3}	0.081	8.85×10^{-5}
	σ	0.20	0.020	0.178	0.93×10^{-3}	0.011	1.11×10^{-5}
BM-WM	$\bar{x}$	1.254	1.354	3.646	4.60×10^{-3}	0.044	5.48×10^{-5}
	σ	0.041	0.023	0.179	0.34×10^{-3}	0.004	0.40×10^{-5}

Table 4. Mean values and standard deviations of the parameters of interest in the triplicate crevice tests in BM and BM-WM in NaCl 3.5% solution (20 ± 2 °C).

		E_R (V)	E_{bd} (V)	i_{pass} (µA/cm²)	i_{Corr} (µA/cm²)	E_{Corr} (V)	C_0 (mm/ano)
BM	$\bar{x}$	1.186	1.339	3.469	0.012	0.036	1.4×10^{-4}
	σ	0.004	0.019	0.341	0.004	0.014	0.5×10^{-4}
BM-WM	$\bar{x}$	1.154	1.252	3.394	0.021	0.071	2.52×10^{-4}
	σ	0.043	0.004	0.525	0.009	0.010	1.07×10^{-4}

3.7. Sample surface analyses after crevice corrosion tests

After the corrosion tests, the surface of the samples was carefully examined. Figure 10a and Figure 10b show macroscopic images obtained by stereomicroscope (Olympus SZX10 series) of the six attacked sites formed under the crevice former in the BM and BM-WM samples subjected to PD-PS-PD tests, respectively. The dotted lines in Figure 10b separate the base metal region (upper and lower part) from the weld metal region (middle).

According to stereoscope images shown in Figure 10, it was observed that during the crevice corrosion tests on both the base metal sample (BM) and the weld metal sample (BM-WM), the crevice former defined a profile irregular localized attack. Note that in the welded sample (Figure 10b), the regions corresponding to BM and WM are marked with horizontal lines. Of these regions, a morphological difference in corrosion can be clearly distinguished, where the WM regions presented a more scattered attack outside the areas limited by the crevice former.

Figure 11a corresponds to the crevice attacked site micrograph (*) of Figure 10a (base metal), while Figure 11b-d show its enlargement. Figure 11c shows that no pits were detected inside these boundaries on the BM sample's surface. Also, it is possible to observe in Figure 11b-d that there was an electrochemical attack that revealed the microstructure of the whole piece surface (with and without contact with the crevice former), as seen by Hang et al.[49] and Yang et al.[50], in many DSS. However, elemental chemical characterizations were carried out using SEM-EDS to differentiate the austenitic phase regions (Cr: 20.75 ± 0.19%wt., Ni: 6.18 ± 0.14%wt., Mo: 2.4 ± 0.08%wt.) from the ferritic ones (Cr: 23.38 ± 0.28%wt., Ni: 3.99 ± 0.23%wt., Mo: 3.7 ± 0.23%wt.). In this regard, it was not possible to identify which phase presented greater susceptibility to corrosion. Both phases were equally consumed at the crevice former boundaries (crevice mouth). Besides, the α/γ, α/α, and γ/γ boundaries were selectively attacked, as shown in Figure 11b and Figure 11d.

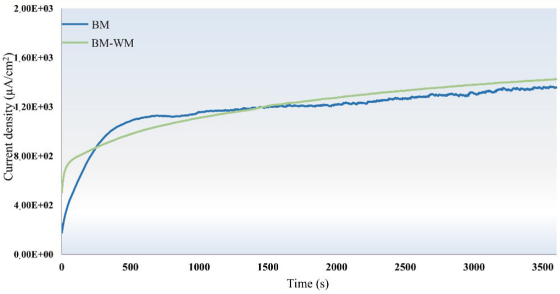

Figure 9. Current density comparative curves as a function of time during the potentiostatic step (PS) in the crevice corrosion test in BM and BM-WM in NaCl 3.5% solution (20 ± 2 °C).

In the crevice corrosion tests, the crevice former generated an opening large enough to allow electrolyte stagnation. Once the solution is in the occluded region, it changes because of the anodic and cathodic reactions until it reaches the critical composition that disrupts the passive film[51]. Finally, the cathodic reactions, mainly oxygen reduction, are inhibited inside the crevice sites because of the oxygen depletion within the crevice and, therefore, are largely confined to the exterior surfaces of the sample (out of the crevice former). Hence, the anodic reactions are limited inside the crevice sites accelerating the dissolution and metal hydrolysis reactions that nucleate at the most susceptible regions, phases, or microstructural defects[51]. Han et al.[49], Zeng et al.[52] and Yang et al.[50], observed that crevice corrosion resistance of ferrite was lower than austenite in neutral NaCl medium for the UNS S31803, UNS S32205, and UNS S32101, respectively. Besides, Torres et al.[53] and Palma Calabokis et al.[41] observed that the initiation of crevice corrosion in 25Cr super DSS started at the grain boundary between phases, followed by selective corrosion of one of the phases depending on the thermochemical treatment. Finally, all studies in DSS agree that the austenite and ferrite phases are equally consumed in the region of greater crevice corrosion depth[41,53,54]. In this work, the base metal samples (BM) presented a similar behavior: corrosion appears to start at grain boundaries, followed by dissolution of both phases, as seen in the magnifications of Figure 11 b,d.

Figure 12 shows the crevice attacked site (**) of Figure 10b formed in the BM-HAZ-WM transition region, indicated by

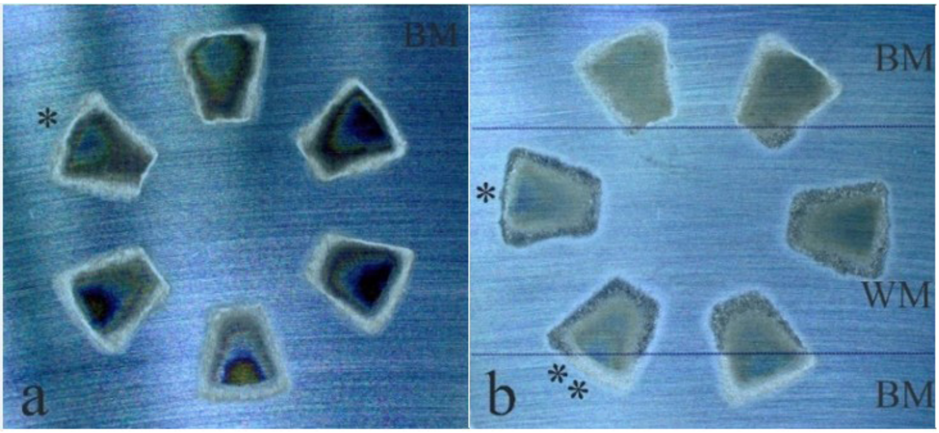

Figure 10. Macrograph of the surface samples in crevice corrosion tests in NaCl 3.5% wt. solution a. Base metal (BM), b. Base metal-weld metal (BM-WM).

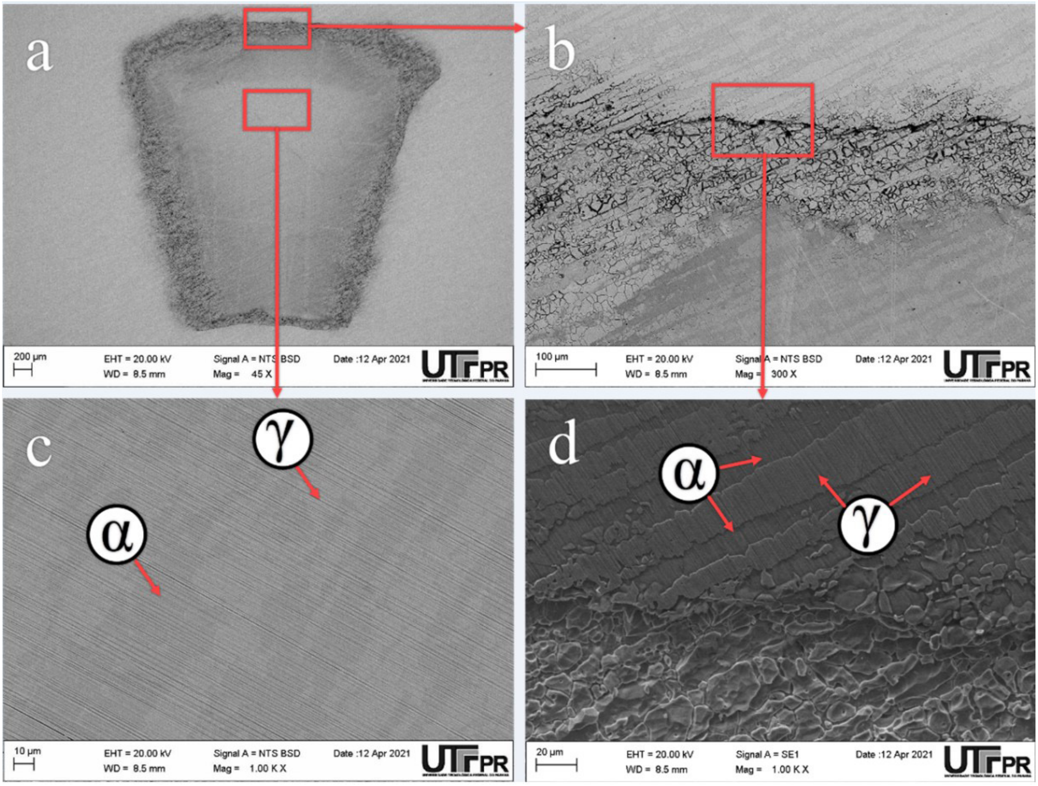

Figure 11. a. SEM micrographs of the crevice attacked site (* in Figure 10a) generated in a BM sample in PD-PS-PD tests in NaCl 3.5% wt. solution. b-d. Magnifications.

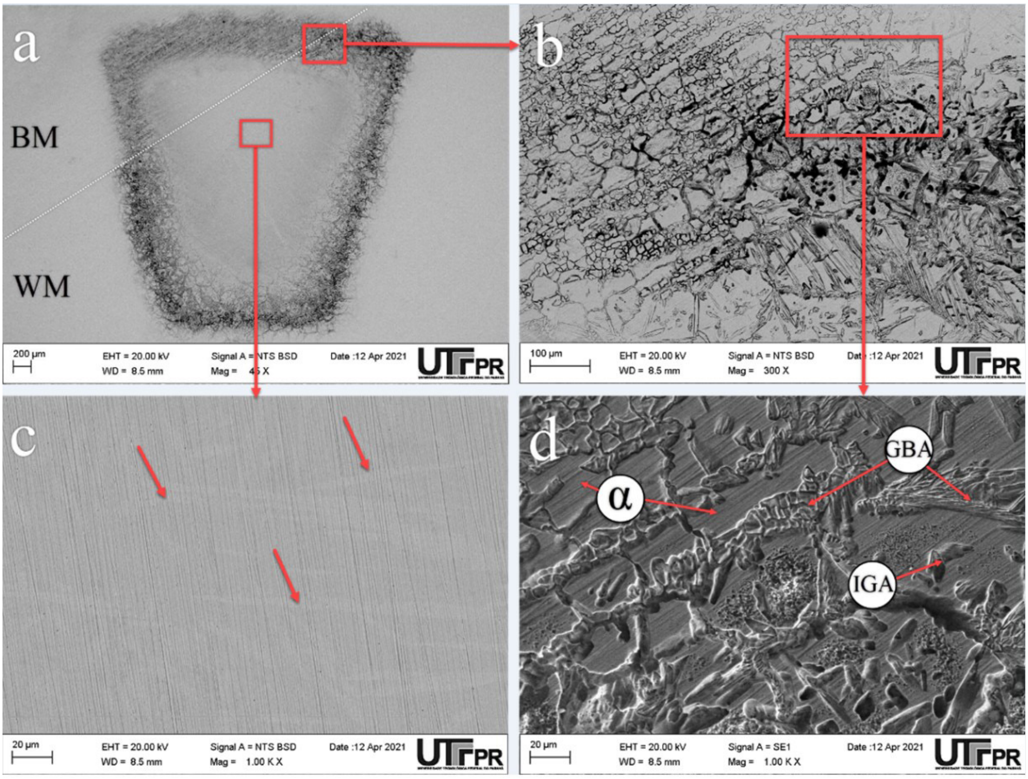

Figure 12. a. SEM micrograph (45X) of the crevice attacked site (** in Figure 10b) generated in a BM-WM sample in PD-PS-PD tests in NaCl 3.5% wt. solution, b-d. Magnifications.

the dotted line in Figure 12a. As seen in BM samples, the electrochemical attack revealed the microstructure of the BM-WM samples (Figure 12c). The arrows in Figure 12c indicated the slightly etched austenite morphologies. In addition, pitting did not occur within the crevice former in the WM zone, as shown in Figure 12c. This fact confirms that the GTAW welding conditions carried out on the DSS UNS S32205 did not affect the pitting corrosion resistance of the alloy, as indicated by the cyclic polarization tests Figure 7.

Figure 12 a,b shows that the crevice corrosion occurred in both the base metal and the weld metal. It could be distinguished in Figure 12b that the corrosion was more intense at the crevice mouth and started at grain boundaries (α/γ), as obtained by Zeng et al.[52] and Yang et al.[50]. Subsequently, as seen in BM samples, the corrosion attack was enlarged to both the outside and the inside of the crevice former boundaries (Figure 12a). Figure 12d and Figure 13 show the preferential dissolution of all morphologies of austenitic phases: grain boundary (GBA), Widmanstätten (WA), and intragranular (IGA). Additionally, notice in Figure 12d and Figure 13 that the regions corresponding to the ferritic phase (matrix) still retain the sanding marks. Zhou et al.[5] confirmed by bipolar electrochemistry tests that a higher susceptibility to transpassive and crevice corrosion occurred in the WM zone of a 2101 lean duplex stainless steel welded using the TIG process. Tests carried out by Zhou et al.[5] did not employ a crevice former, therefore, crevice corrosion did not occur intentionally, it occurred in the interface between the sample and resin. However, according to Zhou et al.[5], higher susceptibility to both types of corrosion was a consequence of the preferential dissolution of secondary austenite in the WM zone, as obtained in this work.

Several studies evaluated the effect of different welding processes on DSS and their consequences to the corrosion resistance by applying electrochemical techniques and solutions containing chlorides[5,14,34-36,42,54]. In general, they reported that the WM and HAZ regions are more susceptible to pitting localized corrosion than the BM, mainly regarding: i) secondary austenite morphologies (IGA, GBA, WA) and deleterious phases, which act as micropits nucleation sites[42,54]; ii) HAZ shows coarser ferrite grains and larger ferrite volume fraction[34]; iii) secondary austenite (IGA, GBA, WA) is more susceptible to corrosion when compared to the primary ferrite and austenite due to its lower Cr, Mo, and N content[14,34,36,42,54]; and iv) change in phase balance (50/50) in WM, and high microstructural heterogeneity[5,34,36]. These four causes were identified for pitting corrosion; however, crevice corrosion is also a type of localized corrosion influenced by the material's microstructural, chemical, and morphological characteristics. In fact, crevice corrosion has not been widely studied in welded duplex stainless steel[5], but in this study, the austenite morphologies (IGA, GBA, WA) in the WM and HAZ regions were heavily and selective corroded compared to the base metal during crevice corrosion (Figure 12, Figure 13).

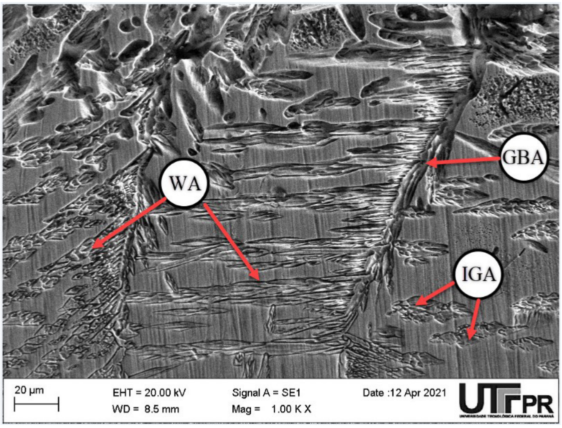

Figure 13. SEM micrograph of the preferential attack of secondary austenite in crevice corrosion tests (PD-PS-PD) generated in the weld metal in NaCl 3.5% wt. solution.

The causes previously listed which promote pit nucleation could be related to the characteristics of the welded DSS UNS S32205 in this study, therefore it can be stated: i) a similar elemental chemical distribution was observed between the austenite morphologies and the ferritic matrix in the WM (Table 1); ii) some changes occurred in the phase balance of the HAZ region (Table 2); iii) high microstructural heterogeneity was also observed in both HAZ and WM regions (Figure 4b, c). Consequently, in this study, the microstructural characteristics of the joints favored preferential corrosion of all the austenite morphologies (Figure 12, Figure 13). Therefore, the WM and HAZ regions were more susceptible to crevice corrosion when compared to the base metal region, as confirmed by Zhou et al.[5].

3.8. Roughness profile

Figure 10 shows that the attack was focused on the crevice former boundaries. By investigating the roughness profile, the severity of the crevice corrosion was analyzed based on the depth of the attack in those regions, as presented in Figure 14. Roughness profiles were measured along the dotted line (as seen in Figure 14b) and across it, always aligned with the axes of symmetry of the crevice former slot.

From Figure. 14b, it is clear the difference in crevice corrosion depth at the crevice mouth between the BM and WM regions. Figure 15 presents the depth average values of the base metal samples (BM samples) and welded samples (BM-WM samples). 'BM region' and 'WM region' (Figure 15) represent the corrosion mean depth in the base metal and weld metal regions of BM-WM samples, both measured separately as indicated by the red and blue rectangles, respectively in Figure 14b. The depth mean values and their confidence intervals were analyzed statistically using a student T-test (confidence = 95%).

The corrosion depth of the 'WM region' (Figure 15) was the most severe, with a mean value statistically higher than that outside the weld bead ('BM region' in Figure 15).

The corrosion depth results (Figure 15) suggested that first, the crevice former formed a macroregion where the electrolyte stagnates. Then, such stagnation speeds the electrolyte acidification until the critical solution composition is reached to initiate and propagate the corrosion. Subsequently, the dissolution and metal hydrolysis reactions occur in the most susceptible phases: the austenite morphologies (Figure 13). Finally, the preferential dissolution of the austenite phases in the weld bead generates localized occluded microregions that

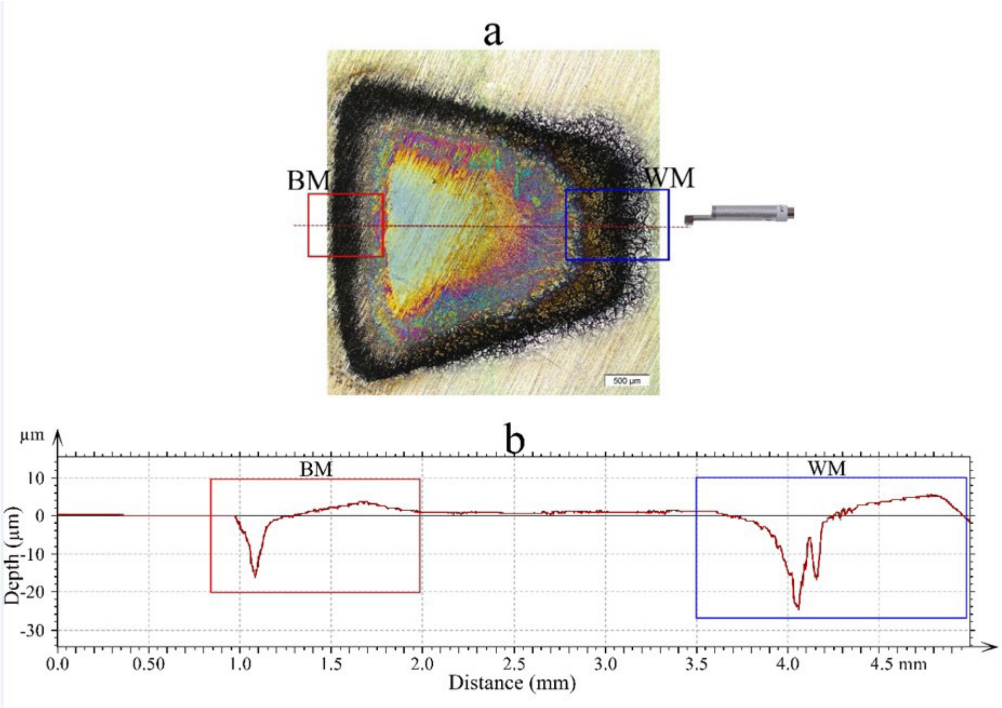

Figure 14. a. Optical micrograph of a crevice corrosion attacked site in the transition between the base metal and the weld metal in welded samples. b. 2D roughness profile measured along the dotted line.

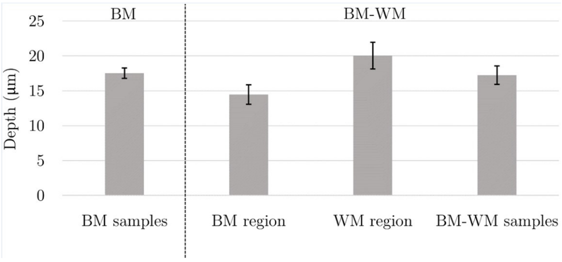

Figure 15. Crevice depth measured with 2D roughness equipment in the BM and BM-WM after the crevice tests. 'BM-WM samples' represent the mean depth along the surface, made up of both the base material, HAZ, and WM regions. 'BM region' and 'WM region' represent the corrosion mean depth in the base material and in the weld metal of welded samples measured separately. Error bars indicated de confidence intervals (Student T-test).

intensify the stagnated condition and accelerates the crevice corrosion attack. Consequently, the crevice corrosion in the WM regions satisfies the critical crevice solution mechanism. However, as observed by Palma Calabokis et al.[41] and Zeng, et al.[52], crevice corrosion attacked in duplex stainless steel occurs in the region known as crevice mouth, also indicating the contribution of the local potential drop mechanism (IR drop) inside the crevice.

It seems relevant to mention that crevice corrosion tests carried out in the BM samples showed mean corrosion depths close to those of the welded samples (BM-WM samples) as seen in Figure 15. Although the microstructure inside the weld metal increases the material susceptibility to crevice corrosion, when the welded BM-WM sample (without separating regions) is evaluated, the different behavior between the base metal and welded samples ended up, presenting little statistical relevance regarding both the attack depth and the electrochemical response. In fact, TAPPI TIP 0402-29[45] and Norsok M-601[46] standards set forth that the susceptibility to corrosion must be evaluated in the welded piece without separating the regions. Thus, the DSS UNS S32205 welded using the GTAW process in this study, showed crevice corrosion resistance comparable to the base material.

4. Conclusions

The GTAW process of DSS UNS S32205 performed in this study kept the material electrochemical behavior of the base metal. This is a consequence of several aspects such as the proper balance of austenite-ferrite phases along the weld metal, the non-formation of precipitates of deleterious phases, and the proper alloy elemental distribution between the base metal and the weld metal.

The austenite morphologies (IGA, GBA, WA) were the localized crevice corrosion preferential nucleation sites in the HAZ and WM regions, catalyzing its propagation inside and outside the crevice formers. Its differentiated behavior occurs due to changes in the austenite/ferrite phase balance in HAZ and the high microstructural heterogeneity in the weld bead (HAZ and WM).

The pitting and crevice corrosion behavior studied by cyclic polarization tests (CP) and step by step tests (PD-PS-PD) in 3.5% NaCl solution demonstrated that no significant differences were found between the base metal and welded samples. The latter was confirmed when the welded piece was evaluated without distinguishing the regions (BM, HAZ, WM) in accordance with the TAPPI TIP 0402-29 and Norsok M-601 standards.

5. Acknowledgments

This work was partially supported by Coordenação de Aperfeiçoamento de Pessoal de Nível Superior (CAPES) for the doctoral sandwich program (PDSE) grant 88881.624474/2021-01. The authors are thankful to the Centro Multiusuário de Caracterização de Materiais (CMCM-UTFPR) for the XRD and SEM-EDS analyses, mainly MSc. Alexandre Gonçalves and PhD Júlio Klein das Neves. P. C. Borges acknowledges CNPq fundings, process 308716/2021-3. The author would also like to acknowledge the special contribution of the company PG CAMPOS for the donation of all materials and the execution of the welding process. The authors also recognize the company ARTIS MATRIZ for the sample grinding.

6. References

1. Rodriguez BR, Miranda A, Gonzalez D, Praga R, Hurtado E. Maintenance of the austenite/ferrite ratio balance in GTAW DSS joints through process parameters optimization. Materials (Basel). 2020;13. http://dx.doi.org/10.3390/ma13030780.
2. Selvabharathi R, Muralikannan R. Influence of shot peening and plasma ion nitriding on tensile strength of 2205 duplex stainless steel using A-PAW. Mater Sci Eng A. 2018;709:232-40. http://dx.doi.org/10.1016/j.msea.2017.10.068.
3. Rodríguez BR, Miranda AF, Hurtado E. Microestructural de la unión disímil de acero inoxidable lean dúplex 2304 y acero inoxidable súper dúplex 2507 soldados mediante el proceso GTAW. In: Congreso 2017 Ingenieria Mecanica/Ciencia E I Ngeniería de Materiales; Septiembre 2017; Querétaro, México. Proceedings. 2017 [cited 2022 Apr 1]. Available from: http://comimsa.repositorioinstitucional.mx/jspui/handle/1022/160
4. Núñez de la Rosa YE, Palma Calabokis O, Borges PC, Ballesteros Ballesteros V. Effect of low-temperature plasma nitriding on corrosion and surface properties of duplex stainless steel UNS S32205. J Mater Eng Perform. 2020;29:2612-22. http://dx.doi.org/10.1007/s11665-020-04753-6.
5. Zhou Y, Kablan A, Engelberg DL. Metallographic screening of duplex stainless steel weld microstructure with a bipolar electrochemistry technique. Mater Charact. 2020;169:110605. http://dx.doi.org/10.1016/j.matchar.2020.110605.
6. Mohammed GR, Ishak M, Aqida SN, Abdulhadi HA. Effects of heat input on microstructure, corrosion and mechanical characteristics of welded austenitic and duplex stainless steels: a review. Metals (Basel). 2017;7. http://dx.doi.org/10.3390/met7020039.
7. Paulraj P, Garg R. Effect of intermetallic phases on corrosion behavior and mechanical properties of duplex stainless steel and super-duplex stainless steel. Adv Sci Technol Res J. 2015;9:87-105. http://dx.doi.org/10.12913/22998624/59090.
8. Badji R, Bacroix B, Bouabdallah M. Texture, microstructure and anisotropic properties in annealed 2205 duplex stainless steel welds. Mater Charact. 2011;62:833-43. http://dx.doi.org/10.1016/j.matchar.2011.06.001.
9. Azzi M, Klemberg-Sapieha J. Tribocorrosion test protocols for sliding contacts. In: Landolt D, Mischler S, editors. Tribocorrosion of passive metals and coatings. Cambridge: Woodhead Pub; 2011. p. 222-38. https://doi.org/10.1533/9780857093738.2.222.
10. Sim BM, Hong TS, Hanim MAA, Tchan EJN, Talari MK. The influence of post weld heat treatment precipitation on duplex stainless steels weld overlay towards pitting corrosion. Materials (Basel). 2019;12. http://dx.doi.org/10.3390/ma12203285.
11. Singh AK, Singh G. Corrosion of stainless steels in chlorine dioxide solution. Anti-Corros Methods Mater. 2002;49:417-25. http://dx.doi.org/10.1108/00035590210452761.
12. Núñez Y, Mafra M, Morales RE, Borges PC, Pintaude G. The effect of plasma nitriding on the synergism between wear and corrosion of SAF 2205 duplex stainless steel. Ind Lubr Tribol. 2020;9:1117-22. http://dx.doi.org/10.1108/ILT-08-2019-0302.
13. Elsaady MA, Khalifa W, Nabil MA, El-Mahallawi IS. Effect of prolonged temperature exposure on pitting corrosion of duplex stainless steel weld joints. Ain Shams Eng J. 2018;9:1407-15. http://dx.doi.org/10.1016/j.asej.2016.09.001.
14. Luchtenberg P, Tancredo P, Campos D, Soares P, Augusto C, Laurindo H et al. Effect of welding energy on the corrosion and tribological properties of duplex stainless steel weld overlay deposited by GMAW/CMT process. Surf Coat Tech. 2019;375:688-93. http://dx.doi.org/10.1016/j.surfcoat.2019.07.072.
15. Badji R, Bouabdallah M, Bacroix B, Kahloun C, Belkessa B, Maza H. Phase transformation and mechanical behavior in annealed 2205 duplex stainless steel welds. Mater Charact. 2008;59:447-53. http://dx.doi.org/10.1016/j.matchar.2007.03.004.
16. Gnanasundaram BR, Natarajan M. Influences of the heat input on a 2205 duplex stainless steel weld. Mater Tehnol. 2014;48:761-3.
17. Zappa S, Zalazar M, Surian E. Efecto de la composición química del metal de aporte y del calor aportado sobre la microestructura y las propiedades mecánicas de juntas soldadas de aceros inoxidables dúplex. Soldag Insp. 2017;22:116-28. http://dx.doi.org/10.1590/0104-9224/SI2202.02.
18. Luo J, Yuan Y, Wang X, Yao Z. Double-sided single-pass submerged arc welding for 2205 duplex stainless steel. J Mater Eng Perform. 2013;22:2477-86. http://dx.doi.org/10.1007/s11665-013-0529-8.
19. Aguiar IV, Escobar DP, Santos DB, Modenesi PJ. Microstructure characterization of a duplex stainless steel weld by electron backscattering diffraction and orientation imaging microscopy techniques. Rev Mat. 2015;20:212-26. http://dx.doi.org/10.1590/S1517-707620150001.0022.
20. Geng S, Sun J, Guo L, Wang H. Evolution of microstructure and corrosion behavior in 2205 duplex stainless steel GTA-welding joint. J Manuf Process. 2015;19:32-7. http://dx.doi.org/10.1016/j.jmapro.2015.03.009.
21. Heider B, Oechsner M, Reisgen U, Ellermeier J, Engler T, Andersohn G et al. Corrosion resistance and microstructure of welded duplex stainless steel surface layers on gray cast iron. J Therm Spray Technol. 2020;29:825-42. http://dx.doi.org/10.1007/s11666-020-01003-y.
22. Tahaei A, Perez AFM, Merlin M, Valdes FAR, Garagnani GL. Effect of the addition of nickel powder and post weld heat treatment on the metallurgical and mechanical properties of the welded UNS S32304 duplex stainless steel. Soldag Insp. 2016;21:197-208. http://dx.doi.org/10.1590/0104-9224/si2102.09.
23. Fonseca CS, Pinheiro IP, Silva SN. Influência do aporte térmico sobre a morfologia da austenita e na quantidade das fases em chapas soldadas de aço inoxidável duplex SAF2205. Materia (Rio J). 2016;21(1):227-34. http://dx.doi.org/10.1590/S1517-707620160001.0020.
24. Roldão AMB. Estudo do efeito do aporte térmico nas propriedades macânicas e microestruturais do aço inoxidável duplex UNS S 31803 em chapa grossa, soldado pelo processo GMAW [thesis]. Belo Horizonte: Universidade Federal de Minas Gerais; 2010.
25. Videira AME. Influência do aporte térmico da soldagem GTAW no balanço de fases ferrita/austenita do aço inoxidável duplex UNS S32205 [dissertation]. Ilha Solteira: Universidade Estadual Paulista; 2016.

26. Nascimento AM, Ierardi MCF, Kina AY, Tavares SSM. Pitting corrosion resistance of cast duplex stainless steels in 3.5%NaCl solution. Mater Charact. 2008;59:1736-40. http://dx.doi.org/10.1016/j.matchar.2008.03.015.
27. Eghlimi A, Shamanian M, Raeissi K. Effect of current type on microstructure and corrosion resistance of super duplex stainless steel claddings produced by the gas tungsten arc welding process. Surf Coat Tech. 2014;244:45-51. http://dx.doi.org/10.1016/j.surfcoat.2014.01.047.
28. Kotecki DJ. Some pitfalls in welding of duplex stainless steels. Soldag Insp. 2010;15:336-43. http://dx.doi.org/10.1590/s0104-92242010000400011.
29. Yousefieh M, Shamanian M, Saatchi A. Influence of heat input in pulsed current GTAW process on microstructure and corrosion resistance of duplex stainless steel welds. J Iron Steel Res Int. 2011;18(9):65-9. http://dx.doi.org/10.1016/S1006-706X(12)60036-3.
30. Moura VS, Lima LD, Pardal JM, Kina AY, Corte RRA, Tavares SSM. Influence of microstructure on the corrosion resistance of the duplex stainless steel UNS S31803. Mater Charact. 2008;59:1127-32. http://dx.doi.org/10.1016/j.matchar.2007.09.002.
31. Vahman M, Shamanian M, Golozar MA, Jalali A, Sarmadi MA, Kangazian J. The effect of welding heat input on the structure–property relationship of a new grade super duplex stainless steel. Steel Res Int. 2020;91:1-12. http://dx.doi.org/10.1002/srin.201900347.
32. Pereira PAS. Efeito da energia de soldagem na microestrutura de um aço inoxidável duplex e super duplex [dissertation]. Campo dos Goytacazes: Universidade Estadual do Norte Fluminense Darcy Ribeiro; 2009.
33. Heider B, Oechsner M, Reisgen U, Ellermeier J, Engler T, Andersohn G et al. Corrosion resistance and microstructure of welded duplex stainless steel surface layers on gray cast iron. J. Therm. Spray Technol. 2020;29:825-42. http://dx.doi.org/10.1007/s11666-020-01003-y.
34. Geng S, Sun J, Guo L, Wang H. Evolution of microstructure and corrosion behavior in 2205 duplex stainless steel GTA-welding joint. J Manuf Process. 2015;19:32-7. http://dx.doi.org/10.1016/j.jmapro.2015.03.009.
35. Eghlimi A, Raeissi K, Shamanian M. Tribocorrosion behavior of overlay welded super duplex stainless steel in chloride medium. J Bio- Tribo-Corros. 2015;1(3):1-15. http://dx.doi.org/10.1007/s40735-015-0018-8.
36. Shin BH, Park S, Park J, Kim D, Hwang M, Chung W. Effect of post-weld heat treatment on the corrosion behavior of resistance spot welded super duplex stainless UNS S 32750. Int J Electrochem Sci. 2019;14:2430-41. http://dx.doi.org/10.20964/2019.03.14.
37. Pettersson R, Westin EM, Johansson M. Corrosion performance of welds in duplex, superduplex and lean duplex stainless steels. In: NACE CORROSION 2013. Proceedings. Texas: OnePetro; 2013.
38. Zhang Z, Jing H, Xu L, Han Y, Zhao L. The influence of microstructural evolution on selective corrosion in duplex stainless steel flux-cored arc welded joints. Corros Sci. 2017;120:194-210. http://dx.doi.org/10.1016/j.corsci.2016.12.007.
39. Palma Calabokis O. Corrosão localizada do aço duplex UNS S32750 nitretado por plasma em baixas temperaturas [dissertation]. Curitiba: Universidade Tecnologica Federal do Paraná; 2020.
40. Videira AM. Influência do aporte térmico da soldagem GTAW no balanço de fases ferrita/austenita do aço inoxidável duplex UNS S32205 [dissertation]. Ilha Solteira: Universidade Estadual Paulista; 2016.
41. Palma Calabokis O, Núñez de la Rosa Y, Lepienski CM, Perito Cardoso R, Borges PC. Crevice and pitting corrosion of low temperature plasma nitrided UNS S32750 super duplex stainless steel. Surf Coat Tech. 2021;413:17-20. http://dx.doi.org/10.1016/j.surfcoat.2021.127095.
42. Zhang Z, Wang Z, Jiang Y, Tan H, Han D, Guo Y et al. Effect of post-weld heat treatment on microstructure evolution and pitting corrosion behavior of UNS S31803 duplex stainless steel welds. Corros Sci. 2012;62:42-50. http://dx.doi.org/10.1016/j.corsci.2012.04.047.
43. Zhang Y, Cheng F, Wu S. Improvement of pitting corrosion resistance of wire arc additive manufactured duplex stainless steel through post-manufacturing heat-treatment. Mater Charact. 2021;171:110743. http://dx.doi.org/10.1016/j.matchar.2020.110743.
44. Singh J, Shahi AS. Electrochemical corrosion behavior and microstructural characteristics of electron beam welded UNS S32205 duplex stainless steel. Mater Corros – Werkst Korros. 2021;72(8):1350-69. http://dx.doi.org/10.1002/maco.202012201.
45. TAPPI. TIP 0402-29: Qualification of welding procedures for duplex stainless steels. Georgia: TAPPI; 2001).
46. Norsok Standard. M-601, Welding and inspection of piping©. Norway: Standards Norway; 2016.
47. Moteshakker A, Danaee I. Microstructure and corrosion resistance of dissimilar weld-joints between duplex stainless steel 2205 and austenitic stainless steel 316L. J Mater Sci Technol. 2016;32:282-90. http://dx.doi.org/10.1016/j.jmst.2015.11.021.
48. Tavares SSM, Pardal JM, Noris LF, Diniz MG. Microstructural characterization and non-destructive testing and of welded joints of duplex stainless steel in flexible pipes. J Mater Res Technol. 2021;15:3399-408. http://dx.doi.org/10.1016/j.jmrt.2021.09.087.
49. Han D, Jiang Y, Deng B, Zhang L, Gao J, Tan H et al. Detecting critical crevice temperature for duplex stainless steels in chloride solutions. Corrosion. 2011;67(2):0250041-7. http://dx.doi.org/10.5006/1.3552290.
50. Yang YZ, Jiang YM, Li J. In situ investigation of crevice corrosion on UNS S32101 duplex stainless steel in sodium chloride solution. Corros Sci. 2013;76:163-9. http://dx.doi.org/10.1016/j.corsci.2013.06.039.
51. Betts AJ, Boulton LH. Crevice corrosion: review of mechanisms, modelling, and mitigation. Br Corros J. 1993;28:279-96. http://dx.doi.org/10.1179/000705993799156299.
52. Zeng H, Yang Y, Liu L, Li M. Pitting and crevice corrosion evolution characteristics of 2205 duplex stainless steel in hot concentrated seawater. J Solid State Electrochem. 2021;25(5):1555-65. http://dx.doi.org/10.1007/s10008-021-04935-9.
53. Torres C, Johnsen R, Iannuzzi M. Crevice corrosion of solution annealed 25Cr duplex stainless steels: effect of W on critical temperatures. Corros Sci. 2021;171:1-14. http://dx.doi.org/10.1016/j.corsci.2020.109053.
54. Zhiqiang Z, Jing H, Xu L, Han Y, Zhao L. The influence of microstructural evolution on selective corrosion in duplex stainless steel flux-cored arc welded joints. Corros Sci. 2017;120:194-210. http://dx.doi.org/10.1016/j.corsci.2016.12.007.